

Article

Effect of Y Content on Precipitation Behavior, Oxidation and Mechanical Properties of As-Cast High-Temperature Titanium Alloys

Jiafeng Shen ¹, Binguo Fu ^{1,2,*} , Yufeng Wang ², Tianshun Dong ¹, Jingkun Li ¹, Guolu Li ¹ and Jinhai Liu ¹

¹ Key Laboratory for New Type of Functional Materials in Hebei Province, School of Materials Science and Engineering, Hebei University of Technology, Tianjin 300401, China; shenjf_1998@163.com (J.S.); dongtianshun111@163.com (T.D.); tjk_zy@126.com (J.L.); liguolu@hebut.edu.cn (G.L.); jhliu57@126.com (J.L.)

² Aerospace Product Center, Tianjin Institute of Aerospace Mechanical and Electrical Equipment, Tianjin 300301, China; wangyufeng_412@163.com

* Correspondence: fubinguohao@163.com

Abstract: To improve the heat resistance of titanium alloys, the effects of Y content on the precipitation behavior, oxidation resistance and high-temperature mechanical properties of as-cast Ti-5Al-2.75Sn-3Zr-1.5Mo-0.45Si-1W-2Nb-xY (x = 0.1, 0.2, 0.4) alloys were systematically investigated. The microstructures, phase evolution and oxidation scales were characterized by XRD, Laser Raman, XPS, SEM and TEM. The properties were studied by cyclic oxidation as well as room- and high-temperature tensile testing. The results show that the microstructures of the alloys are of the widmanstätten structure with typical basket weave features, and the prior β grain size and α lamellar spacing are refined with the increase of Y content. The precipitates in the alloys mainly include Y_2O_3 and $(TiZr)_6Si_3$ silicide phases. The Y_2O_3 phase has specific orientation relationships with the α -Ti phase: $(002)_{Y_2O_3} // (\bar{1}\bar{1}20)_{\alpha-Ti}$, $[110]_{Y_2O_3} // [4401]_{\alpha-Ti}$. $(TiZr)_6Si_3$ has an orientation relationship with the β -Ti phase: $(02\bar{2}1)_{(TiZr)_6Si_3} // (011)_{\beta-Ti}$, $[\bar{1}2\bar{1}6]_{(TiZr)_6Si_3} // [044]_{\beta-Ti}$. The 0.1 wt.% Y composition alloy has the best high-temperature oxidation resistance at different temperatures. The oxidation behaviors of the alloys follow the linear-parabolic law, and the oxidation products of the alloys are composed of rutile-TiO₂, anatase-TiO₂, Y₂O₃ and Al₂O₃. The room-temperature and 700 °C UTS of the alloys decreases first and then increases with the increase of Y content; the 0.1 wt.% Y composition alloy has the best room-temperature mechanical properties with a UTS of 1012 MPa and elongation of 1.0%. The 700 °C UTS and elongation of the alloy with 0.1 wt.% Y is 694 MPa and 9.8%, showing an optimal comprehensive performance. The UTS and elongation of the alloys at 750 °C increase first and then decrease with the increase of Y content. The optimal UTS and elongation of the alloy is 556 MPa and 10.1% obtained in 0.2 wt.% Y composition alloy. The cleavage and dimples fractures are the primary fracture mode for the room- and high-temperature tensile fracture, respectively.

Keywords: high-temperature titanium alloy; Y content; precipitated phases; oxidation behavior; mechanical property



Citation: Shen, J.; Fu, B.; Wang, Y.; Dong, T.; Li, J.; Li, G.; Liu, J. Effect of Y Content on Precipitation Behavior, Oxidation and Mechanical Properties of As-Cast High-Temperature Titanium Alloys. *Materials* **2023**, *16*, 4784. <https://doi.org/10.3390/ma16134784>

Academic Editor: Guozheng Quan

Received: 7 June 2023

Revised: 23 June 2023

Accepted: 30 June 2023

Published: 2 July 2023



Copyright: © 2023 by the authors. Licensee MDPI, Basel, Switzerland. This article is an open access article distributed under the terms and conditions of the Creative Commons Attribution (CC BY) license (<https://creativecommons.org/licenses/by/4.0/>).

1. Introduction

High-temperature titanium alloys are widely used in aerospace and military fields due to their excellent properties, such as low density, high specific strength, high specific stiffness and excellent high-temperature creep properties [1–3]. With the development of aerospace vehicles towards higher flight speeds, in addition to requiring titanium alloys with low density and high strength, they are also required to withstand higher temperatures [4,5]. At present, the maximum service temperature of titanium alloys used for a long period can reach 600 °C. Typical brands are Ti-1100, IMI834, BT36, Ti60 and Ti600 alloys [6,7]. However, when an aerospace vehicle flies at supersonic speeds, it has strong

friction with the air, generating extremely high heat. The surface material temperature can be maintained at 700 °C for a short period of time, which may have a serious impact on the structural integrity of the aircraft [8]. Therefore, there is an urgent need to develop 700 °C short-term high-temperature titanium alloy for manufacturing high-temperature components of aircraft. Fully utilizing the matching effect of various alloy elements is one of the important methods for developing and improving the microstructure and properties of cast high-temperature titanium alloys. Alloying elements in titanium alloys are usually classified into α or β stabilizing additions depending on whether they increase or decrease the α/β transformation temperature of pure Ti. Currently, the composition design for high-temperature titanium alloys with temperatures up to 600 °C is the Ti-Al-Sn-Zr-Mo-Si series [9,10]. Some studies have suggested that the addition of β -stabilizer elements W and Nb can further increase its usage temperature [11–13]; however, the increase in service temperature is limited.

The rare earth element Y has strong chemical activity and deoxidation, which can purify the titanium alloy matrix and improve the high-temperature mechanical properties and oxidation resistance of the alloy. Y mainly affects the microstructures of titanium alloys by forming the Y_2O_3 phase, thereby improving their strength and toughness [14–16]. Previous studies have pointed out that the addition of rare earth elements to a Ti-Al-Sn-Zr-Mo-Si series titanium alloy could refine the oxide particles and improve the oxidation resistance of the alloy [17]. Therefore, the addition of the Y element to the high-temperature titanium alloys may be an effective method to improve the heat resistance. However, the precipitation behavior of the Y_2O_3 phase, as well as the interaction between Y and other alloy elements and the mechanism of their impact on the high-temperature properties of the alloys are still unclear.

In this present work, the effect of Y content (0.1, 0.2, 0.4 wt.%) on the precipitation behavior, oxidation and mechanical properties of the as-cast Ti-Al-Sn-Zr-Mo-Si-W-Nb series high-temperature titanium alloys were systematically investigated. In addition, the corresponding oxidation and high-temperature fracture mechanism were also discussed.

2. Materials and Methods

Ti-5Al-2.75Sn-3Zr-1.5Mo-0.45Si-1W-2Nb-xY ($x = 0.1, 0.2, 0.4$) alloys, developed for the application at 700 °C based on traditional design methods for near α titanium alloys, were prepared by the vacuum electromagnetic levitation melting technique. Pure Ti, Y, Al, Zr, Sn, Mo, Nb and Si were added in the form of elemental alloys, and W was added in the form of a Ti-90W master alloy. Melting stocks weighing 1 kg were melted in a water-cooled copper crucible. Before melting, the sealed evacuated chamber was washed three times with 99.999% high-purity argon, and the internal atmosphere environment was controlled below 10^{-3} Pa. The melting process was at a dry high-purity argon (99.999%) atmosphere maintained at 5×10^3 Pa. After the raw materials were melted uniformly, the melt was kept for 2 min and then cooled to room temperature in the crucible. Each ingot was melted four times to keep the composition homogeneity. The actual compositions of the prepared titanium alloys were analyzed by an X-ray fluorescent spectrometer (XRF, Panalytical, Almelo, The Netherland), and the results were given in Table 1.

Table 1. Actual chemical compositions of as-cast Ti-5Al-2.75Sn-3Zr-1.5Mo-0.45Si-1W-2Nb-xY alloys (wt.%).

Alloys	Al	Sn	Zr	Mo	Si	W	Nb	Y	Ti
0.1 wt.% Y	4.54	2.57	2.73	1.40	0.42	1.09	2.05	0.13	Bal.
0.2 wt.% Y	4.67	2.89	2.85	1.47	0.46	1.07	2.07	0.28	Bal.
0.4 wt.% Y	4.58	2.90	2.87	1.48	0.52	1.14	2.07	0.39	Bal.

The specimens for microstructure characterization, oxidation and mechanical performance tests were cut by wire-cut electrical discharge machining (WEDM). The phases and

oxidation products of the as-cast alloys were characterized by a Smartlab (9 kW) X-ray diffractometer (XRD, Rigaku, Akishima, Japan) with a scanning speed of $10^\circ/\text{min}$. The microstructure, oxidation morphology and tensile fracture of the alloys were observed by the Quanta 450-FEG type scanning electron microscope (SEM, FEI, Eindhoven, The Netherlands) equipped with an energy dispersive X-ray spectrometer (EDS, FEI, Eindhoven, The Netherlands). The precipitates were characterized by a Tecnai G2 F30 transmission electron microscope (TEM, FEI, Amsterdam, The Netherlands). The oxidation mechanisms were analyzed by LabRAM HR Evolution type laser Raman (LRS, HORIBA, Kyoto, Japan) and ESCALAB 250 Xi X-ray photoelectron spectroscopy (XPS, TMO, NY, USA). Specimens for SEM observations were etched with Kroll's reagent ($\text{HF}:\text{HNO}_3:\text{H}_2\text{O} = 1:3:7$, Vol.%). TEM observation specimens were ground to $40\ \mu\text{m}$ and then punched to $\Phi 3\ \text{mm}$ discs for ion thinning.

The high-temperature oxidation resistance test was carried out in a KSL-1100X type medium temperature box resistance furnace (HF-Kejing, Hefei, China) at $650\ ^\circ\text{C}$, $700\ ^\circ\text{C}$ and $750\ ^\circ\text{C}$. The dimensions of the oxidation specimen were $10 \times 10 \times 3\ \text{mm}^3$. Each specimen was measured by a vernier caliper, and the surface area was recorded. The specimen for the oxidation resistance test was placed in a dried corundum crucible, and the weight of the specimen and crucible was measured by an electronic balance with an accuracy of $0.01\ \text{mg}$ as the initial weight before the test. The whole oxidation test lasted for 120 h, and the crucible was taken out every 12 h to obtain the weight changes. Three specimens were placed in each group to calculate the average weight gain value to improve the measurement accuracy.

The room-temperature tensile test was implemented on an Instron-5848 (Boston, MA, USA) tensile testing machine at a tensile rate of $1\ \text{mm}/\text{min}$. According to the ASTM E8/E8M-16 standard, a 15 mm gauge length extensometer was used to measure the strain to exclude the influence of the elastic strain of the grips. The high-temperature tensile test was carried out on the CMT-5205 tensile testing machine in the air environment at $700\ ^\circ\text{C}$ and $750\ ^\circ\text{C}$. The tensile rate was $0.5\ \text{mm}/\text{min}$. The tensile test was repeated three times under each condition. The dimensions of the tensile specimens for room- and high-temperature tests are shown in Figure 1.

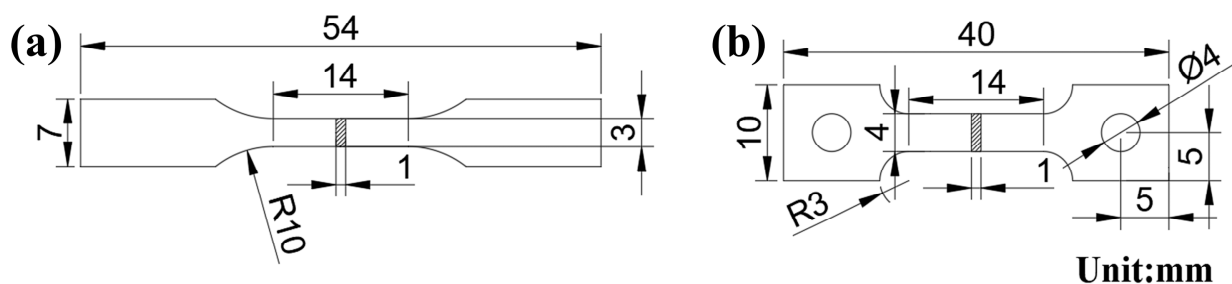


Figure 1. Geometric dimension of the specimens for (a) room-temperature tensile test; and (b) high-temperature tensile test.

3. Results and Discussion

3.1. Microstructure

Figure 2 shows the XRD spectra of the as-cast Ti-5Al-2.75Sn-3Zr-1.5Mo-0.45Si-1W-2Nb-xY ($x = 0.1, 0.2, 0.4$) alloys. It can be seen that the as-cast alloys are mainly composed of close-packed hexagonal (hcp) α -Ti phase and a small amount of body-centered cubic (bcc) β -Ti phase, and all the alloys still belong to near- α titanium alloy. It also can be observed that the increase of Y content promotes the diffraction peak of the α -Ti phase to move to a low angle direction. According to the Bragg's equation [11], the shift of the diffraction peak to a low angle is caused by lattice expansion. The lattice parameters of the α -Ti phase in 0.1 wt.%, 0.2 wt.% and 0.4 wt.% Y composition alloys were obtained by XRD refinement, and the averages of three measurement results are $a = 0.2914\ \text{nm}$, $c = 0.4643\ \text{nm}$; $a = 0.2923\ \text{nm}$, $c = 0.4678\ \text{nm}$; and $a = 0.2920\ \text{nm}$, $c = 0.4687\ \text{nm}$, respectively. It can be seen

that both the lattice parameter “a” and “c” increase due to the Y with large atomic radius substituting for Ti atoms with small atomic radius, with the increase of Y content.

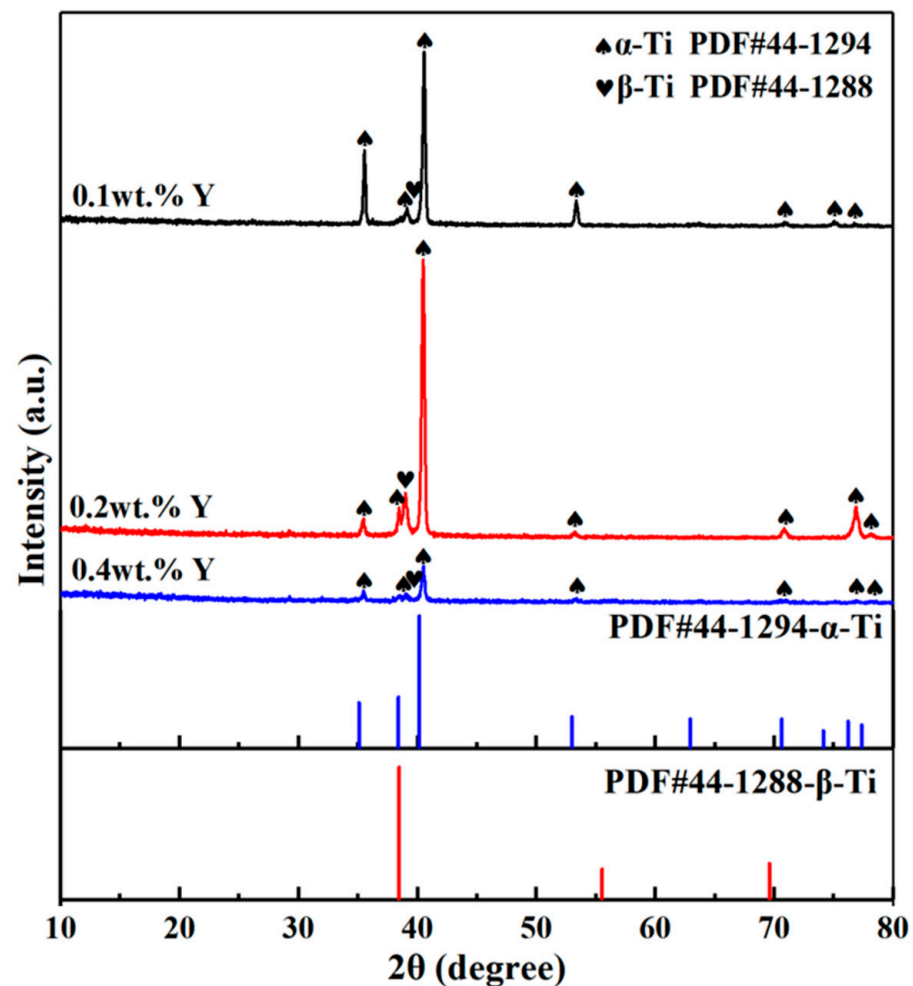


Figure 2. XRD patterns of as-cast titanium alloys with different Y content.

Figure 3 shows the SEM microstructures of the as-cast alloys with different Y content. It can be seen that all the microstructures are of the Widmanstätten structure, with typical basket weave features. The prior β grains in the microstructure are relatively coarse, and they are composed of lamellar α -Ti and residual β -Ti phases. The prior β grain size and α lamellar spacing decrease with the increase of Y content. The addition of the Y element can improve the energy state of the structure; thus, the grains in the microstructures have more growth orientations, resulting in a typical basket weave feature. It also can be observed that some white precipitates are distributed at the prior β grain boundaries. As the Y content increases, the morphologies of the precipitates change from short rod to long strip, and they gradually form a network distribution along the prior β grain boundaries. The number of precipitates increases with the increase of Y content. According to the EDS results presented in Table 2, it can be determined that the precipitates are Y_2O_3 phase.

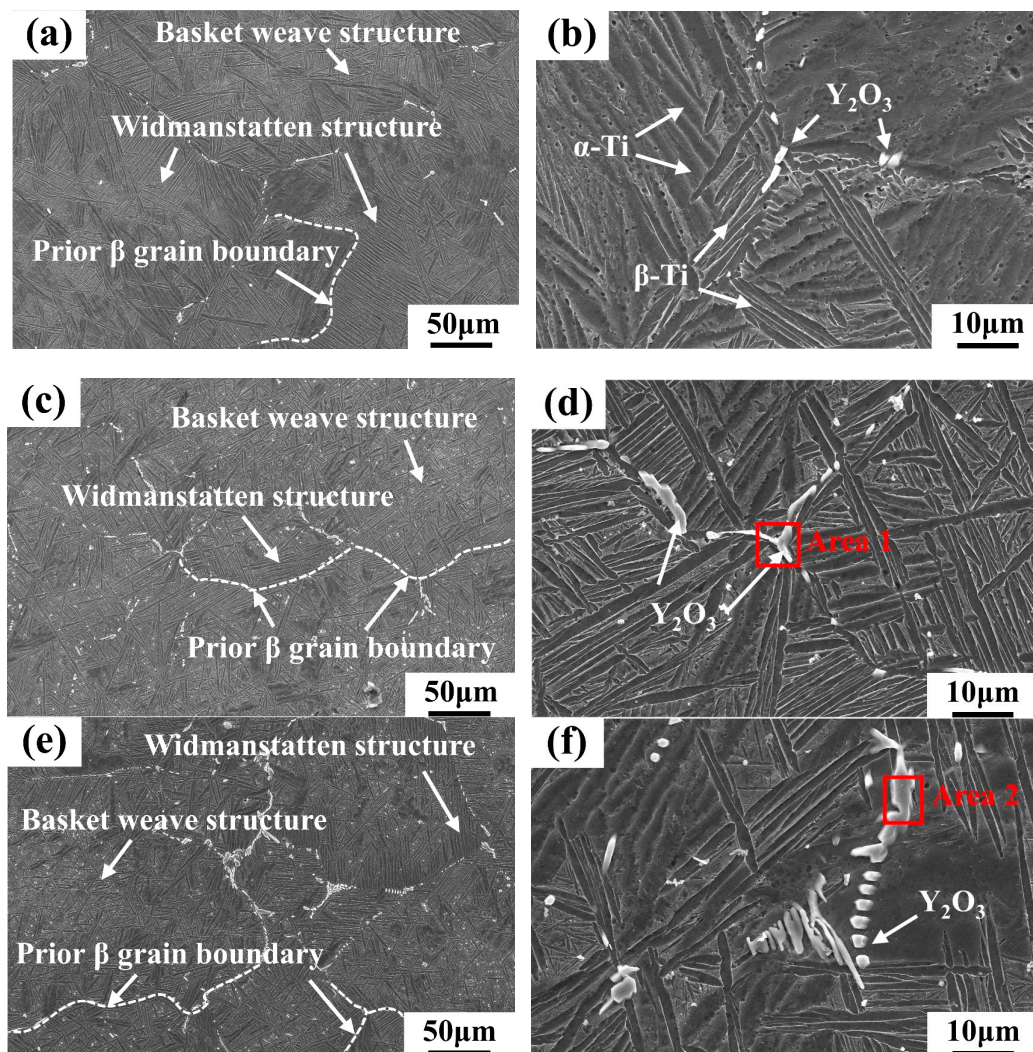


Figure 3. SEM microstructures of the as-cast alloys with different Y content: (a,b) 0.1 wt.% Y; (c,d) 0.2 wt.% Y; (e,f) 0.4 wt.% Y.

Table 2. EDS analysis results of areas 1 and 2 marked in Figure 3 (at.%).

Position	Ti	Al	Y	O	Nb	Sn	Zr	Mo	Si	W
Area 1	1.75	0.18	40.75	57.14	0.13	0.05	-	-	-	-
Area 2	2.45	0.33	37.19	55.32	0.07	0.20	3.25	0.18	0.26	0.75

Figure 4 shows the TEM images of the alloys with Y content of 0.1 wt.% and 0.2 wt.%. It can be seen that the ellipsoidal precipitates with an average size of about 20–60 nm distributed near the β phases (Figure 4a,c) [18,19]. According to the selected area electron diffraction (SAED) analysis presented in Figure 4b,d, the precipitated phase is hexagonal $(\text{TiZr})_6\text{Si}_3$ silicide (S_2 , $a = 0.701$ nm, $c = 0.370$ nm). The addition of the Y element in the alloys will reduce the solid solubility of Si in the β phases and promote the precipitation of silicides. It also can be seen that the $(\text{TiZr})_6\text{Si}_3$ silicide has an orientation relationship with the β -Ti phase: $(02\bar{2}1)_{(\text{TiZr})_6\text{Si}_3} // (011)_{\beta\text{-Ti}}$, $[1\bar{2}16]_{(\text{TiZr})_6\text{Si}_3} // [044]_{\beta\text{-Ti}}$ (Figure 4b). Figure 4e shows the high-resolution transmission electron microscopy (HRTEM) image of the interfacial structure between the $(\text{TiZr})_6\text{Si}_3$ silicide and α -Ti phase [20,21]. It can be seen that the interface between the $(\text{TiZr})_6\text{Si}_3$ silicide and α -Ti phase is clean, without defects, and it belongs to a semi-coherent relationship.

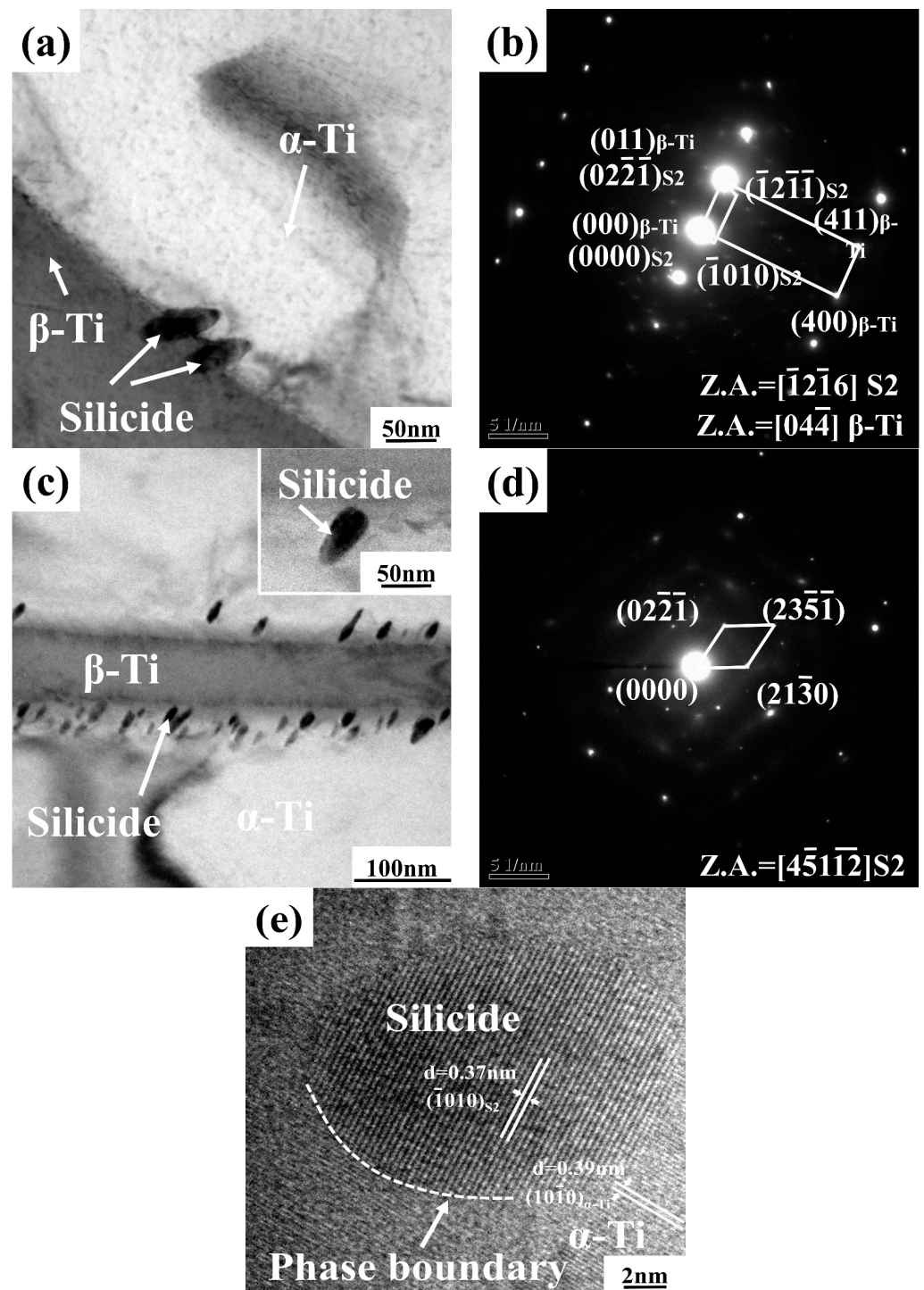


Figure 4. (a) Bright field TEM image of the as-cast alloy with 0.1 wt.% Y; (b) SAED pattern of the silicide taken from (a); (c) Bright field TEM image of the as-cast alloy with 0.2 wt.% Y; (d) SAED pattern of the silicide taken from (c); (e) HRTEM image of silicide in as-cast alloy with 0.1 wt.% Y.

3.2. Y_2O_3 Precipitation

Figure 5 shows the TEM images of the as-cast alloys with 0.1 wt.% and 0.4 wt.% Y content. It can be seen that the massive particles, with a size of about 300–400 nm, precipitated from the β phase (Figure 5a,c). They can be indexed as Y_2O_3 phase according to the SAED analyses (Figure 5b,d). The orientation relationships between Y_2O_3 phase and α -Ti phase in 0.1 wt.% Y composition alloy are established as: $(002)_{Y_2O_3} // (\bar{1}\bar{1}20)_{\alpha\text{-Ti}}$, $[110]_{Y_2O_3} // [\bar{4}401]_{\alpha\text{-Ti}}$.

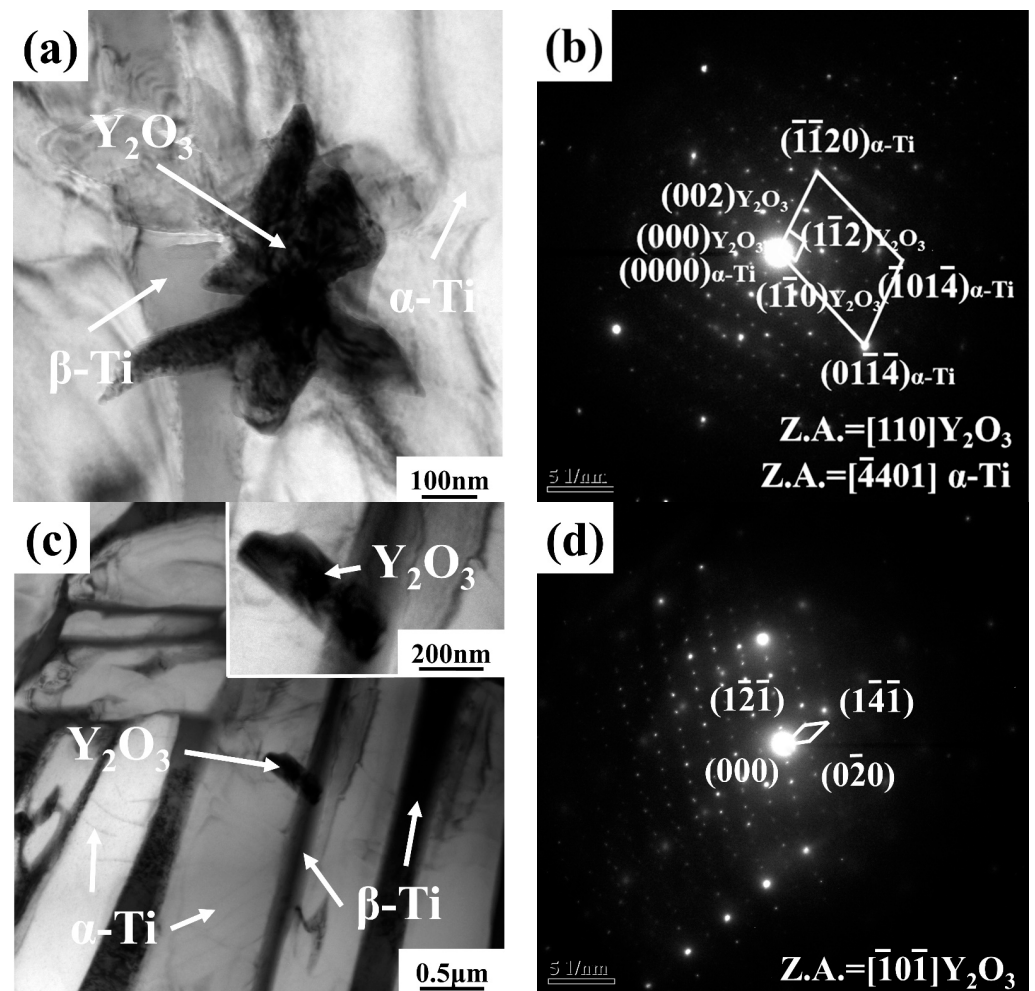


Figure 5. (a) Bright field TEM image of the Y_2O_3 in the as-cast alloy with 0.1 wt.% Y; (b) SAED pattern of the Y_2O_3 taken from (a); (c) Bright field TEM image of the Y_2O_3 in the as-cast alloy with 0.4 wt.% Y; (d) SAED pattern of the Y_2O_3 taken from (c).

The solid solubility of the Y element in titanium alloy is low, and it has strong chemical activity and deoxidation, which can capture the interstitial oxygen in the Ti matrix to form the Y_2O_3 phase [22]. Figure 6 sketches the possible solidification path of the high-temperature titanium alloys containing Y. It can be seen that the Y_2O_3 phase can be directly formed in the liquid phase due to its higher melting point than the titanium alloy. As the solidification temperature decreases, the β phase forms, and some Y_2O_3 phases can serve as a heterogeneous nucleation site for the β phase, improving its nucleation rate. In this case, the Y_2O_3 phase in the remaining liquid phase will be pushed into the interdendritic region of the β phase. Therefore, most Y_2O_3 phases would eventually be distributed at the prior β grain boundaries. As the temperature continues to decrease, the silicide phase will precipitate from the β phase; then, β/α transformation occurs. Thus, the Y_2O_3 phase can cooperate with the silicide phase to produce a pinning effect on grain boundaries and improve the mechanical properties of the alloy at high temperatures.

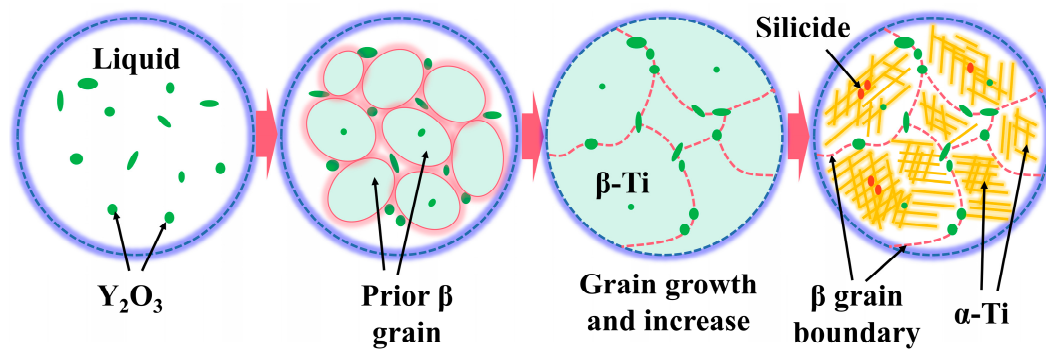


Figure 6. Schematic view of solidification path of the high-temperature titanium alloy containing Y.

3.3. Oxidation Resistance

Figure 7 illustrates the oxidation weight gain curves of as-cast alloys with different Y content, oxidized at different temperatures for up to 120 h. It can be seen that the oxidation weight gain of alloys with different Y content increases with the increase of oxidation time. The oxidation weight gain of alloys increases with the increase of oxidation temperature at the same Y content. Further increase in Y content under the same conditions has adverse effects on the oxidation resistance of the alloy. The oxidation weight gain per unit area of as-cast alloys with different Y content at different temperatures for 120 h is shown in Table 3. Combined with the analysis in Figure 7, the 0.1 wt.% Y composition alloy has the smallest weight gain value and the best high-temperature oxidation resistance.

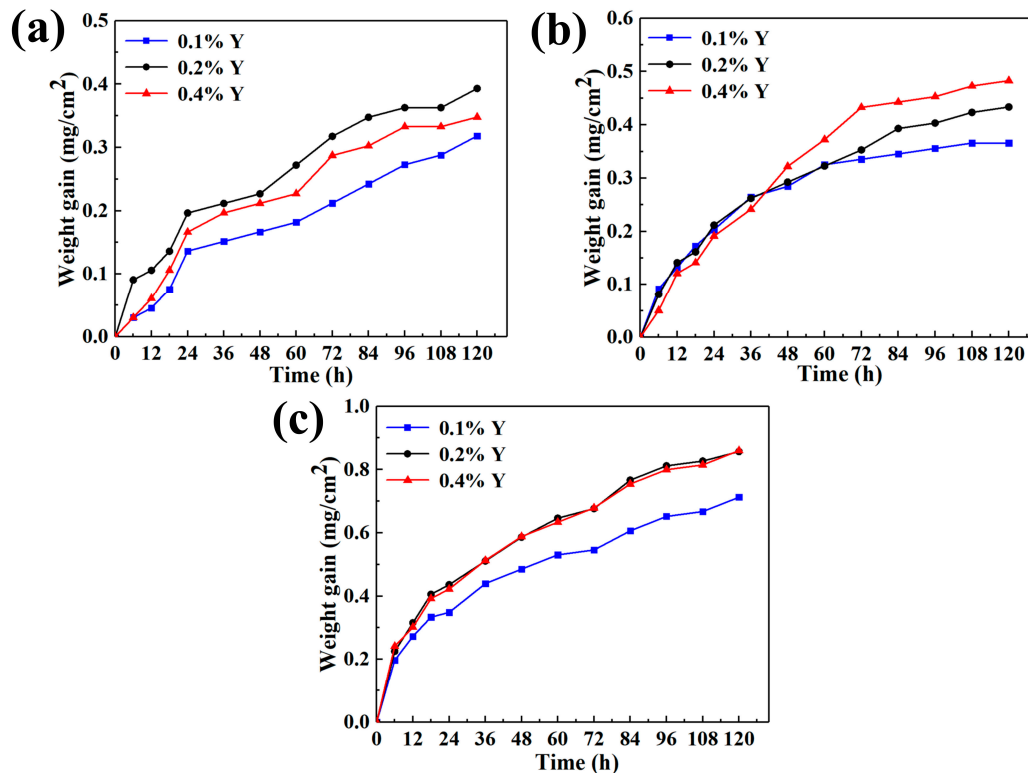


Figure 7. Oxidation weight gain curves of as-cast alloys with different Y content varying with oxidation time at different temperatures: (a) 650 °C; (b) 700 °C; (c) 750 °C.

Table 3. Oxidation weight gain per unit area of as-cast alloys with different Y content at different temperatures for 120 h (mg/cm²).

Alloy	650 °C	700 °C	750 °C
0.1 wt.% Y	0.318	0.366	0.713
0.2 wt.% Y	0.393	0.433	0.857
0.4 wt.% Y	0.348	0.483	0.860

The oxidation kinetics can be expressed by Equation (1) [23]:

$$\Delta W^n = k_n t \quad (1)$$

where ΔW is the oxidation weight gain (mg/cm²), n is the reaction index, k_n is the oxidation reaction rate constant, and t is the oxidation time (s). Equation (1) is subjected to natural logarithm processing to obtain Equation (2):

$$n \lg(\Delta W) = \lg k_n + \lg t \quad (2)$$

This demonstrates that there is a linear relationship between $\lg(\Delta W)$ and $\lg t$, and n and k_n can be used as parameters to characterize the oxidation behaviors of materials. The fitting parameters of the alloys at each oxidation temperature are provided in Table 4. It can be seen that the oxidation reaction index n of the alloy is between 1 and 2, which shows that the oxidation of the alloys is controlled by diffusion process [24,25] and the oxidation weight gain of the alloy follows the linear-parabolic law.

Table 4. The oxidation reaction index (n) and reaction rate constant (k_n) of alloys with different Y content at different temperatures for 120 h.

Temperature/°C	Alloy	n	k_n
650	0.1 wt.% Y	1.2933	1.99×10^{-3}
	0.2 wt.% Y	1.9178	1.42×10^{-3}
	0.4 wt.% Y	1.2804	2.66×10^{-3}
700	0.1 wt.% Y	2.1187	1.28×10^{-3}
	0.2 wt.% Y	1.8295	2.07×10^{-3}
	0.4 wt.% Y	1.3637	3.85×10^{-3}
750	0.1 wt.% Y	2.3956	3.62×10^{-3}
	0.2 wt.% Y	2.2684	6.19×10^{-3}
	0.4 wt.% Y	2.3051	5.94×10^{-3}

Figure 8 shows the XRD patterns of the as-cast alloys with different Y content after being oxidized at different temperatures for 60 h and 120 h. It can be seen that the oxidation products of the as-cast alloys are mainly rutile-TiO₂, Al₂O₃ and Y₂O₃. The lattice constants of α -Ti after oxidation were calculated according to the XRD data, and the results are exhibited in Table 5. It can be seen that both the lattice constant 'a' and 'c' of the as-cast alloys after oxidation increase, which is caused by the entry of small-sized oxygen atoms into the lattice gap during the oxidation process [26,27]. With the increase of oxidation temperature and time, some interstitial oxygen in the lattice is consumed form oxidation products. Thus, the degree of lattice expansion will be reduced.

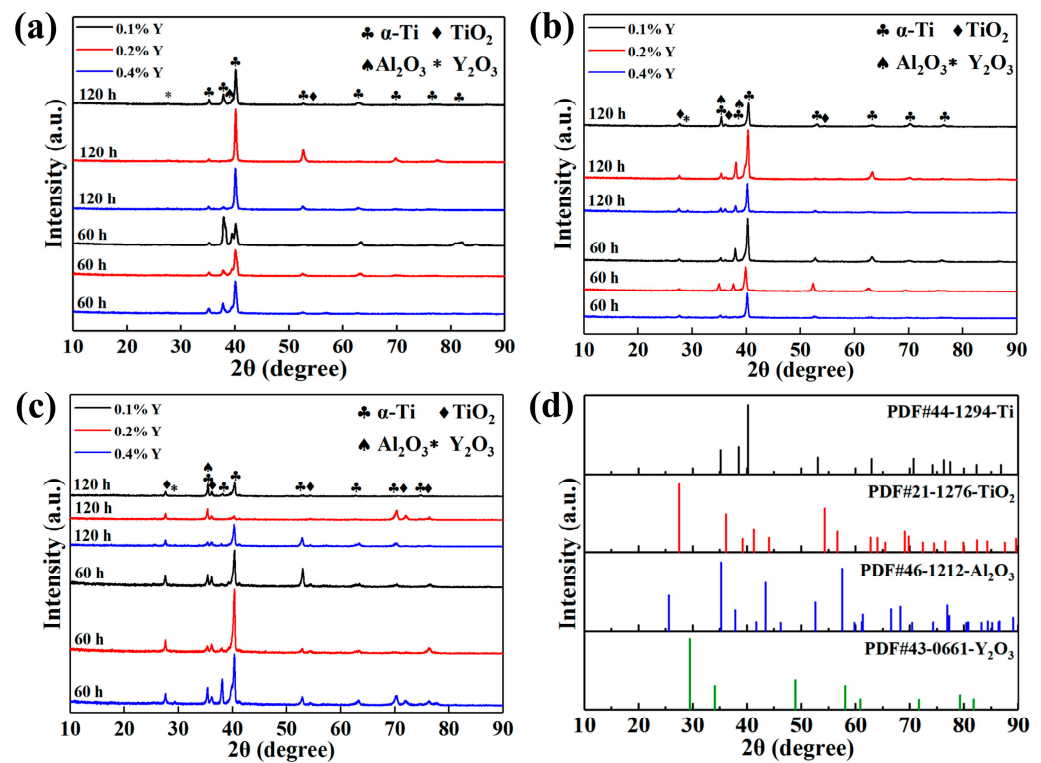


Figure 8. XRD patterns of the as-cast alloys with different Y content after being oxidized at different temperatures for 60 h and 120 h: (a) 650 °C; (b) 700 °C; (c) 750 °C; (d) standard spectrum.

Table 5. Lattice constant of α -Ti of the as-cast alloys with different Y content before and after being oxidized at different temperatures for 60 h and 120 h.

Alloy	Temperature/°C	a (0.1–0.2–0.4 wt.%Y)/nm	c (0.1–0.2–0.4 wt.%Y)/nm
As-cast	25	0.29136–0.29233–0.29198	0.46426–0.46780–0.46871
60 h Oxidation	650	0.29376–0.29485–0.29482	0.47020–0.47185–0.47443
	700	0.29377–0.29626–0.29473	0.47253–0.47755–0.47292
	750	0.29304–0.29350–0.29311	0.46983–0.47020–0.47068
120 h Oxidation	650	0.29415–0.29434–0.29516	0.47452–0.47568–0.47413
	700	0.29284–0.29289–0.29421	0.46932–0.47185–0.47257
	750	0.29253–0.29302–0.29397	0.46997–0.47317–0.46895

To further analyze the compositions of the surface oxidation products, LRS and XPS tests were conducted. The 0.2 wt.% Y composition alloy oxidized at 650 °C for 120 h and 0.4 wt.% Y composition alloy oxidized at 700 °C and 750 °C for 120 h were selected for the laser Raman test in the range of 100–1000 cm^{-1} . The corresponding laser Raman spectra are displayed in Figure 9. It can be seen that the oxidation products are composed of rutile-TiO₂ (238 cm^{-1} , 448 cm^{-1} , 608 cm^{-1}), anatase-TiO₂ (143 cm^{-1}), Y₂O₃ (312 cm^{-1}) and Al₂O₃ (378 cm^{-1}) [28]. However, anatase-TiO₂ was not found in the XRD analysis (Figure 8) due to its low content and easy encapsulation by rutile-TiO₂.

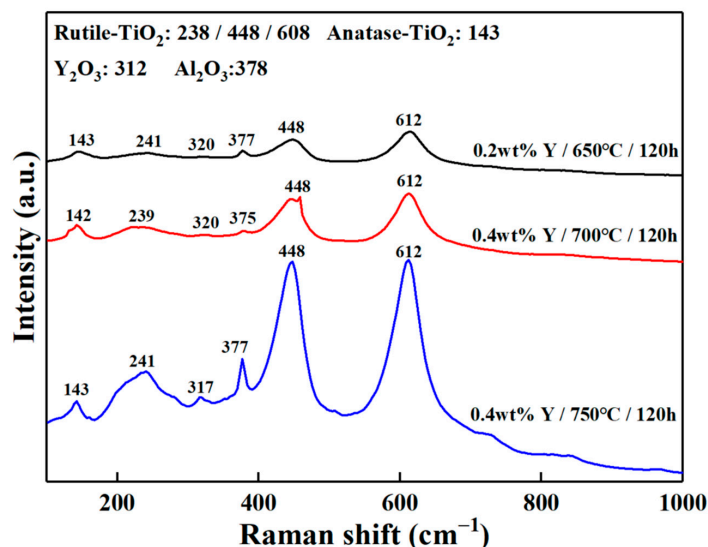


Figure 9. Laser Raman spectra of 0.2 wt.% Y composition alloy oxidized at 650 °C for 120 h and 0.4 wt.% Y composition alloy oxidized at 700 °C and 750 °C for 120 h.

Figure 10 illustrates the XPS spectra of 0.4 wt.% Y composition alloy oxidized at 750 °C for 120 h. It can be seen that the valence states of elements in the oxidation products are Ti^{4+} (458.62 eV, 464.62 eV), Al^{3+} (74.76 eV, 74.42 eV), O^{2-} (529.88 eV, 531.99 eV) and Y^{3+} (158.5 eV, 157.0 eV) [29]. Among them, O^{2-} with a binding energy of 529.88 eV and 531.99 eV is oxygen in titanium oxide and alumina, respectively. Ti^{4+} with a binding energy of 458.62 eV and 464.62 eV is titanium in anatase- TiO_2 and rutile- TiO_2 , respectively. The fitting results of XPS are consistent with the results of laser Raman and XRD analysis. Therefore, it can be considered that the oxidation products of the alloy are composed of rutile- TiO_2 , anatase- TiO_2 , Y_2O_3 and Al_2O_3 .

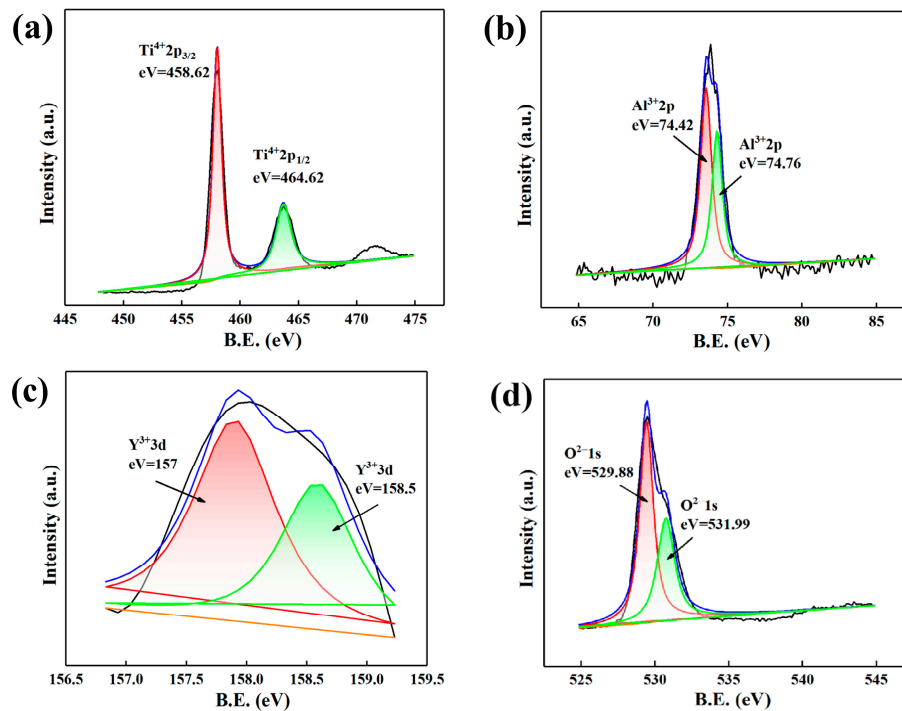


Figure 10. XPS spectra of 0.4 wt.% Y composition alloy oxidized at 750 °C for 120 h: (a) Ti2p; (b) Al2p; (c) Y3d; (d) O1s.

Figure 11 shows the surface morphology of as-cast alloys with different Y content after oxidation for 120 h at different temperatures. EDS analysis results of the oxidation surface marked in Figure 11 are listed in Table 6. It can be seen that the oxidation surfaces are mainly composed of granular TiO_2 , short rod Y_2O_3 and Al_2O_3 . The oxide particles on the surface of the alloys oxidized at $650\text{ }^\circ\text{C}$ are smaller, and no serious cracks are observed on the oxidized surfaces. As the oxidation temperature exceeds $700\text{ }^\circ\text{C}$, the amount and size of the oxide particles increases significantly. Therefore, stress would occur between the oxide particles and the matrix, causing cracks. These cracks provide a large number of channels for the internal diffusion of oxygen atoms, which is not conducive to the formation of a uniform and dense oxide film. When the oxidation temperature exceeds $750\text{ }^\circ\text{C}$, the integrity of the oxide layer is seriously damaged. Thus, the oxidation resistance of the alloy decreases with the increase of oxidation temperatures. The number and size of oxidation products increase with the increase of Y content, further indicating that the 0.1 wt.% Y composition alloy has the best high-temperature oxidation resistance.

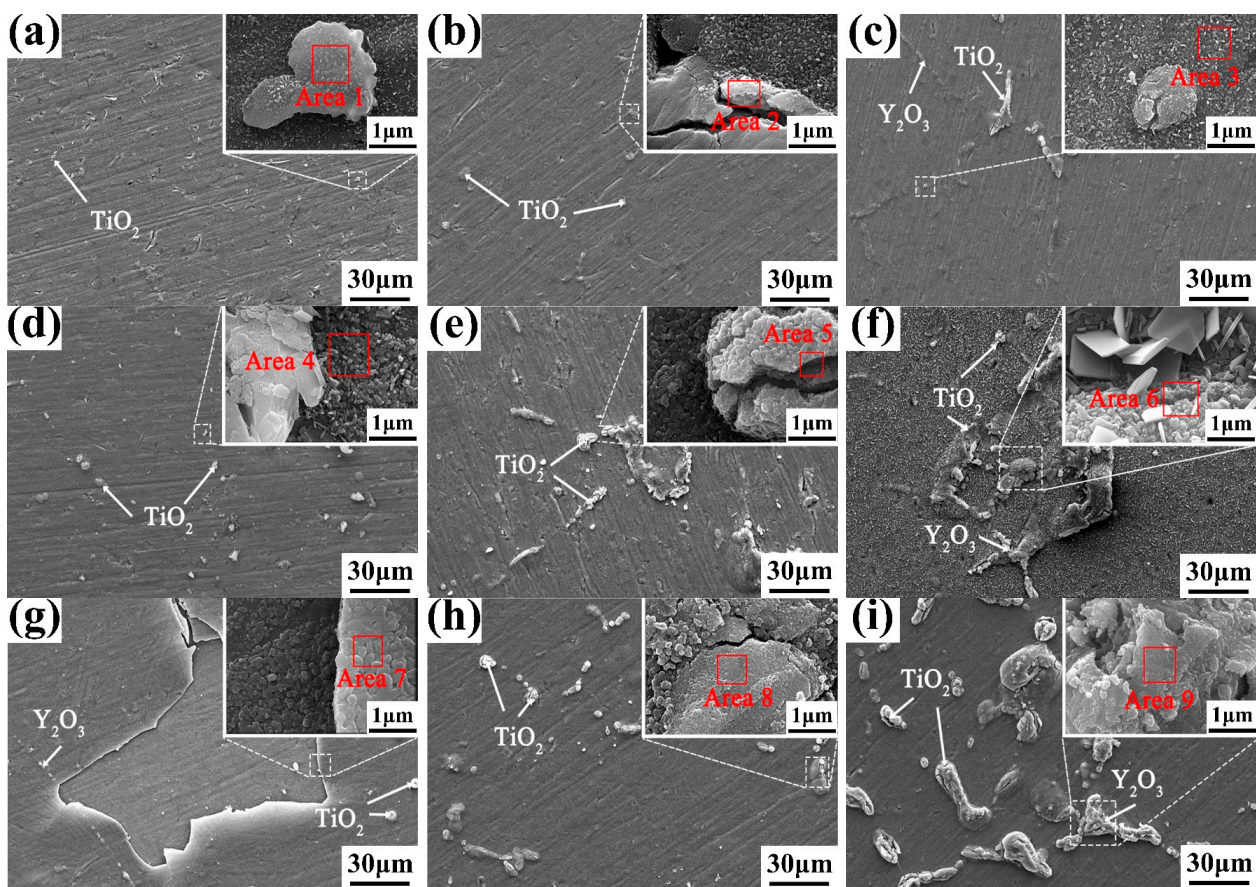


Figure 11. Surface morphology of the (a,d,g) 0.1 wt.% Y; (b,e,h) 0.2 wt.% Y; and (c,f,i) 0.4 wt.% Y alloys oxidized at (a–c) $650\text{ }^\circ\text{C}$; (d–f) $700\text{ }^\circ\text{C}$; and (g–i) $750\text{ }^\circ\text{C}$ for 120 h.

Table 6. EDS analysis results of the oxidation surface marked in Figure 11 (wt.%).

Position	Ti	Al	Y	O	Zr	Nb	Mo
Area 1	55.16	5.48	0.40	35.26	1.83	1.62	0.25
Area 2	35.77	4.17	6.46	45.10	3.02	5.11	0.37
Area 3	59.02	5.59	0.06	27.25	2.70	4.97	0.41

Table 6. Cont.

Position	Ti	Al	Y	O	Zr	Nb	Mo
Area 4	45.59	5.52	0.02	40.73	2.13	5.89	0.12
Area 5	51.08	5.43	0.11	35.28	2.66	5.21	0.23
Area 6	43.55	5.68	0.01	44.24	2.35	3.91	0.26
Area 7	75.48	3.93	0.11	10.10	2.19	7.77	0.42
Area 8	18.14	2.50	42.30	23.72	2.76	10.19	0.39
Area 9	38.95	9.33	8.12	33.23	2.66	7.37	0.34

To further explore the change process of the oxide layer in different oxidation stages, the surface morphologies of as-cast alloys with different Y content after oxidation for 60 h at different temperatures were characterized, and the results are presented in Figure 12. EDS analysis results of the oxidation surface marked in Figure 12 are listed in Table 7. It can be seen that the morphology of the surface oxide particles under 60 h and 120 h oxidation is similar; however, there are fewer surface cracks and oxide spalling under 60 h oxidation. This indicates that the external oxide layer has been basically formed after 60 h of oxidation. After 60 h, the oxidation mainly enters the internal diffusion stage of O atoms, which can damage the density and integrity of the oxide film.

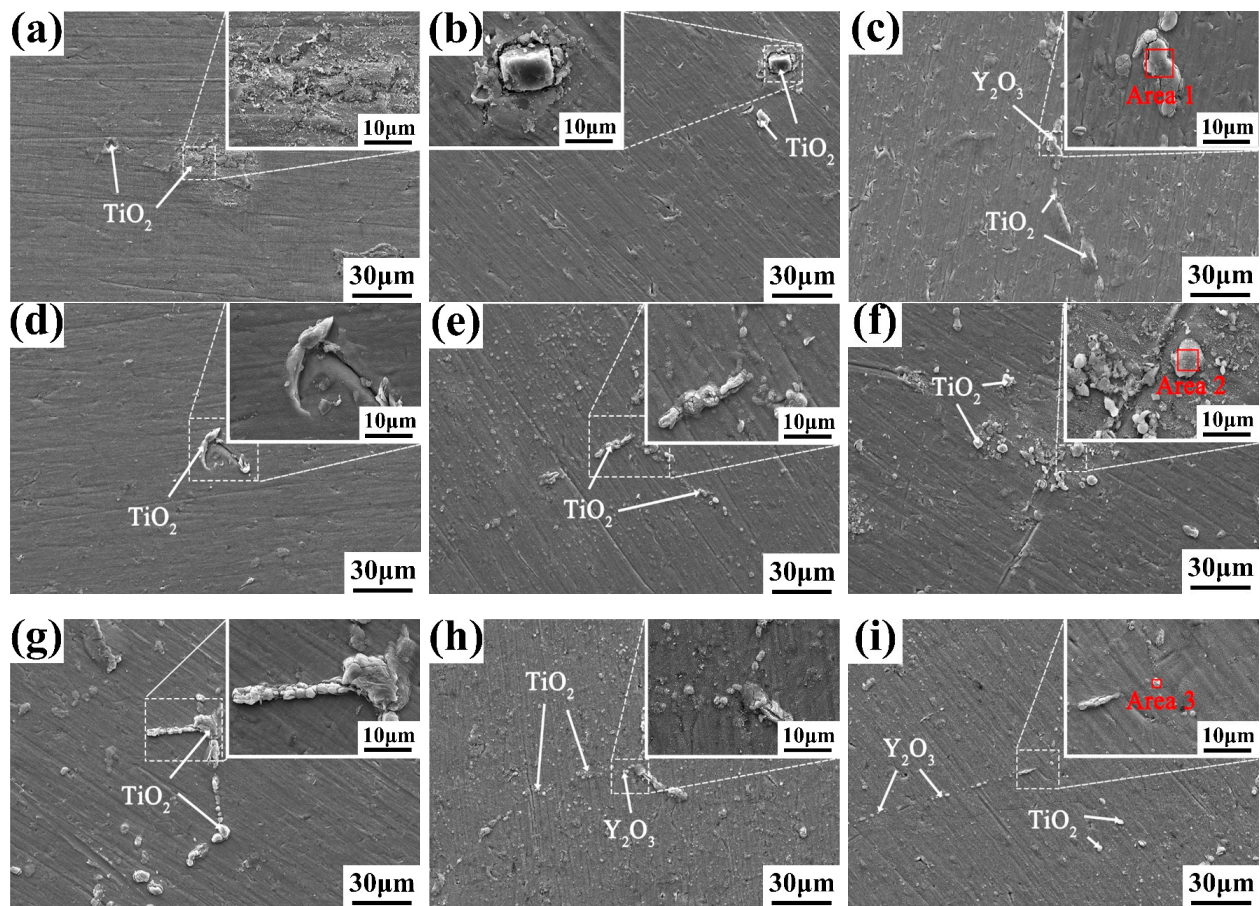


Figure 12. Surface morphology of the (a,d,g) 0.1 wt.% Y; (b,e,h) 0.2 wt.% Y; and (c,f,i) 0.4 wt.% Y alloys oxidized at (a–c) 650 °C; (d–f) 700 °C; and (g–i) 750 °C for 60 h.

Table 7. EDS analysis results of the oxidation surface marked in Figure 12 (wt.%).

Position	Ti	Al	Y	O	Zr	Nb	Mo
Area 1	20.00	2.49	35.36	33.24	2.31	5.89	0.71
Area 2	42.50	4.15	0.29	46.27	1.93	4.59	0.27
Area 3	39.57	3.96	4.39	43.49	3.95	4.28	0.36

To further study the composition of oxidation products, thermodynamic analysis was carried out. The oxidation reaction of titanium alloy follows the Vant Hoff isothermal equation, as specified in Equation (3) [30]:

$$\Delta G = \Delta G_0 - RT \ln P_{O_2} \quad (3)$$

where ΔG is the Gibbs free energy change, ΔG_0 is the standard free energy change. R is the gas constant, T is the Kelvin temperature, and P_{O_2} is the equilibrium oxygen partial pressure. As described above, TiO_2 and Al_2O_3 are the main oxidation products. The ΔG of TiO_2 and Al_2O_3 at 650 °C, 700 °C and 750 °C is calculated according to Equation (3), and the results are listed in Table 8. It can be seen that Al_2O_3 and TiO_2 can coexist on the oxide surface due to their ΔG value being negative. The stability of Al_2O_3 is also higher than that of TiO_2 . However, TiO_2 was easier to form due to the much higher content of Ti than Al.

Table 8. Gibbs free energy change (ΔG) of TiO_2 and Al_2O_3 at different temperatures ($kJ \cdot mol^{-1}$).

ΔG	650 °C	700 °C	750 °C
TiO_2	−750	−742	−733
Al_2O_3	−1381	−1365	−1349

Figures 13–15 show the cross-section morphologies and elemental distribution curves of the oxidation surfaces of as-cast alloys with different Y content for different temperatures under oxidation for 120 h. It can be seen that the oxidation profile can be divided into the surface oxide film, oxide layer and matrix. The surface oxide film is difficult to distinguish due to its extremely thin thickness. The thickness of the oxide layer of the alloys with different Y content oxidized at different temperatures for 120 h is illustrated in Table 9. It can be seen that under the same oxidation temperature conditions, the 0.1 wt.% Y composition alloy has the smallest oxide layer thickness, further proving that it has the best oxidation resistance. According to the elemental distribution line scan and thermodynamic calculations analysis, it can be seen that Al_2O_3 is mainly distributed in the outermost layer of the oxide film, the inner layer of the oxide film is mainly composed of TiO_2 and a small amount of Al_2O_3 , and the oxide layer is mainly TiO_2 . This shows that in the early stage of oxidation, Ti and Al elements diffuse outward and oxidation reaction occurs; the generated oxides cover Y_2O_3 to form an oxide film with a loose structure. With the extension of oxidation time, oxygen atoms can diffuse inward through the gaps and cracks in the oxide film and oxidize with Ti atoms inside the matrix to form an oxygen-rich layer. Due to the different types of oxidation products in the oxide surface and oxide layer, the stress concentration generated means that the oxide film and the oxide layer cannot be tightly bonded, resulting in the oxide layer being peeled off at more than 750 °C.

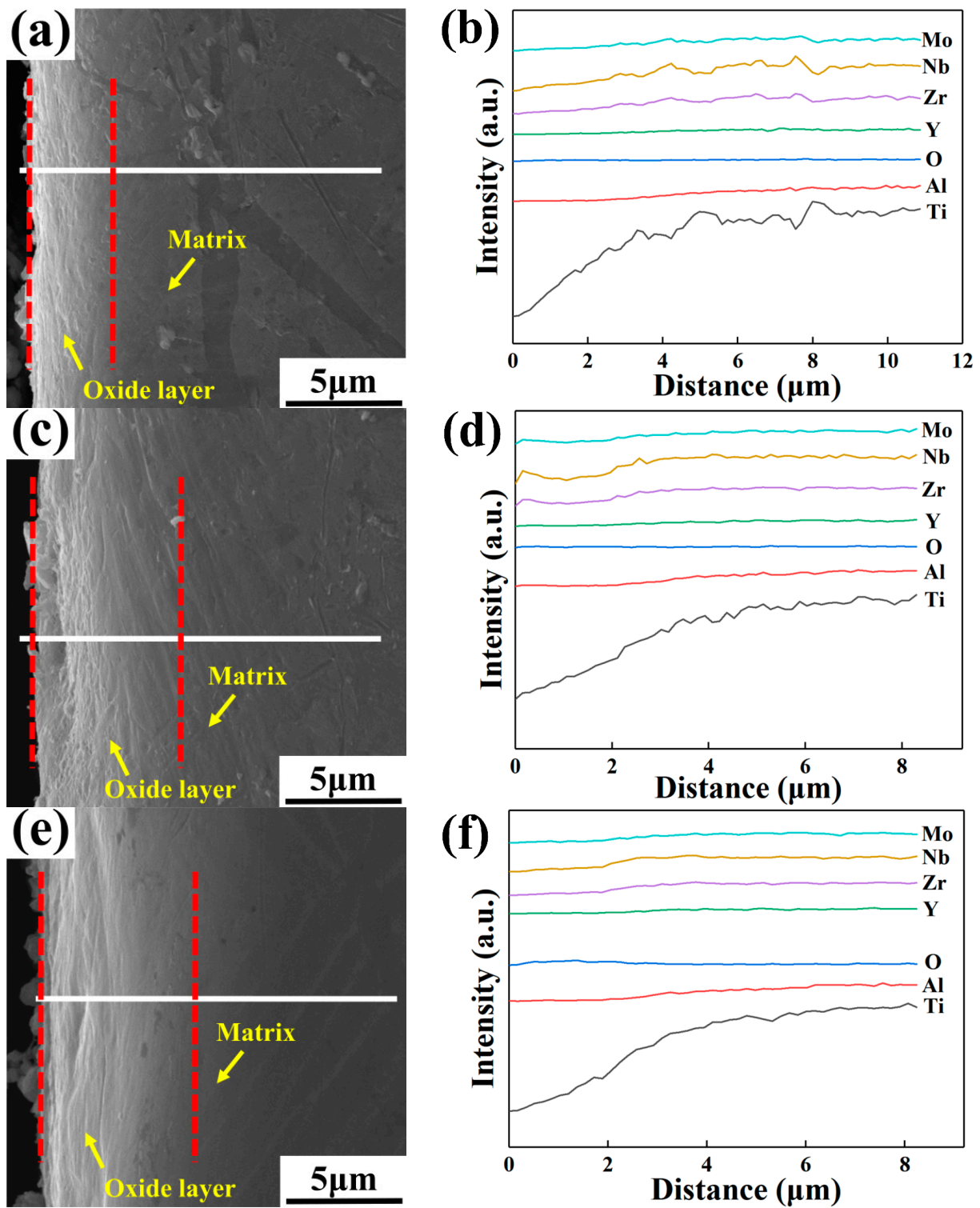


Figure 13. Cross-section morphologies and elemental distribution curves of the oxidation surfaces of as-cast alloys with different Y content after oxidation for 120 h at 650 °C: (a,b) 0.1 wt.% Y; (c,d) 0.2 wt.% Y; (e,f) 0.4 wt.% Y.

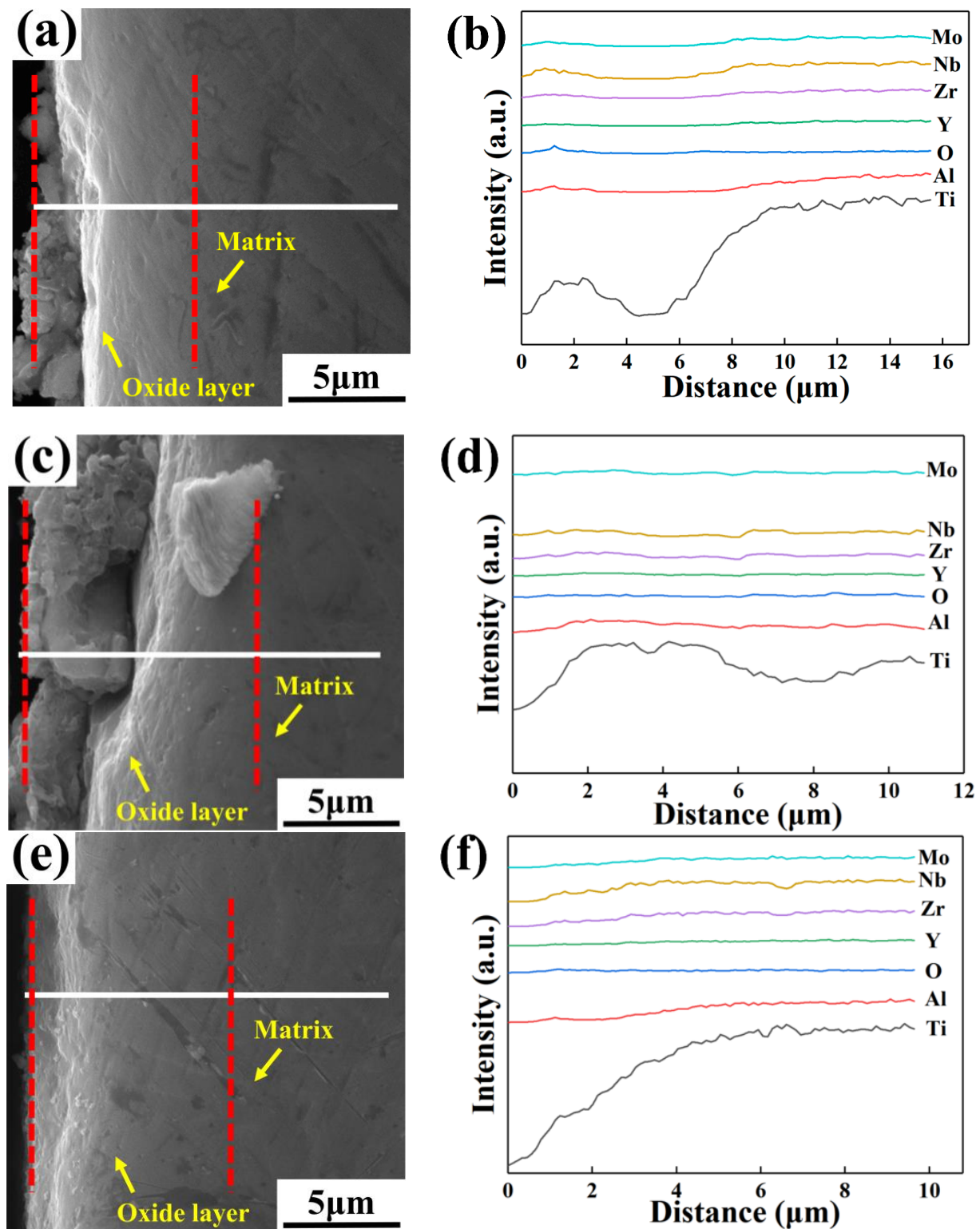


Figure 14. Cross-section morphologies and elemental distribution curves of the oxidation surfaces of as-cast alloys with different Y content after oxidation for 120 h at 700 °C: (a,b) 0.1 wt.% Y; (c,d) 0.2 wt.% Y; (e,f) 0.4 wt.% Y.

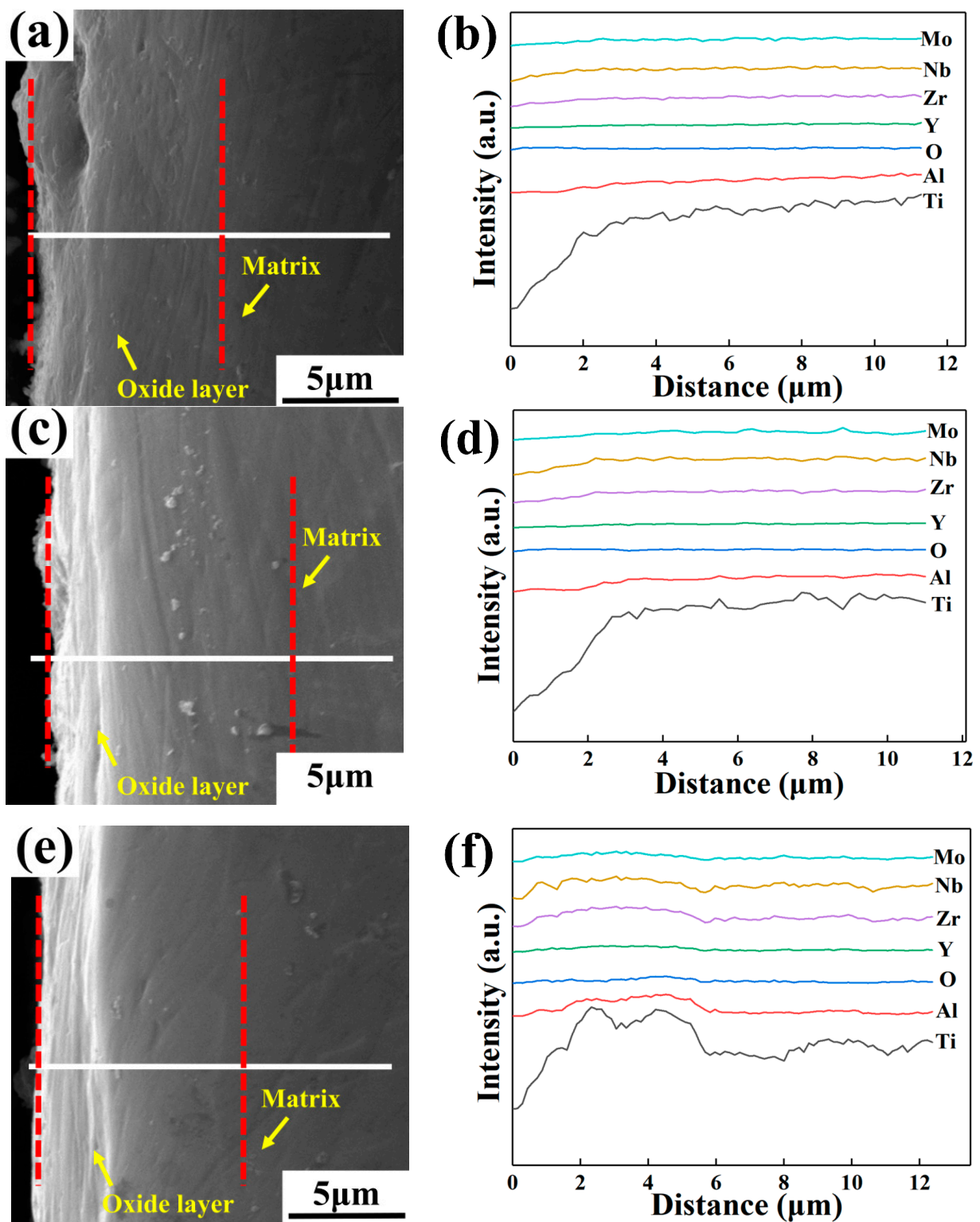


Figure 15. Cross-section morphologies and elemental distribution curves of the oxidation surfaces of as-cast alloys with different Y content after oxidation for 120 h at 750 °C: (a,b) 0.1 wt.% Y; (c,d) 0.2 wt.% Y; (e,f) 0.4 wt.% Y.

Table 9. The oxide layer thickness of as-cast alloys with different Y content oxidized at different temperatures for 120 h (μm).

Temperature/ $^{\circ}\text{C}$	0.1 wt.% Y	0.2 wt.% Y	0.4 wt.% Y
650	4.9	6.2	6.4
700	7.8	10.2	8.6
750	10.2	11.3	10.6

3.4. Mechanical Properties

Figure 16 shows the room-temperature tensile engineering stress–strain curves of the alloys with different Y content, and Table 10 lists the corresponding values of the mechanical properties. It can be seen that the elongation of the cast alloys are all less than 1%, and the engineering stress–strain curves of the alloys at room temperature are all close to straight lines, indicating that the material behavior can be considered as brittle. The ultimate tensile strength (UTS) of the alloys decreases first and then increases with the increase of Y content. The alloy with 0.1 wt.% Y content has the best comprehensive mechanical properties at room temperature, and the UTS and elongation (EL) are 1012 MPa and 1.0 %, respectively. Figure 17 shows the high-temperature tensile stress–strain curves of the alloys with different Y content. Combined with the data in Table 10, it can be seen that the UTS of the alloys at 700 $^{\circ}\text{C}$ decreases first and then increases with the increase of Y content, whereas the elongation shows an opposite trend. The UTS and elongation of the alloy with 0.1 wt.% Y is 694 MPa and 9.8%, showing an optimal comprehensive performance. The UTS and elongation of the alloys at 750 $^{\circ}\text{C}$ increase first and then decrease with the increase of Y content. The UTS and elongation of the alloy with 0.2 wt.% Y content are 556 MPa and 10.1%, which is 4.5%, 17.4% and 5.3%, 17.4% higher than that of the alloy with 0.1 wt.% and 0.4 wt.% Y content, respectively.

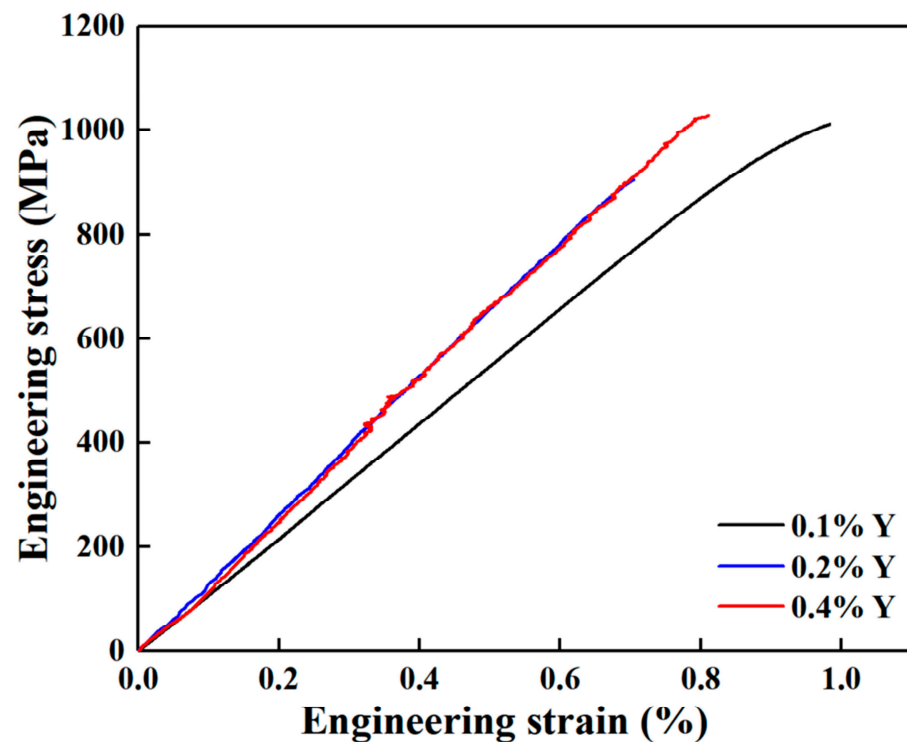
**Figure 16.** Room-temperature tensile stress–strain curves of as-cast alloys with different Y content.

Table 10. Room and high-temperature mechanical properties of the as-cast alloys with different Y content.

Temperature/°C	Alloy	UTS/MPa	EL/%
25	0.1 wt.% Y	1012 ± 5.7	1.0 ± 0.05
	0.2 wt.% Y	906 ± 2.1	0.7 ± 0.03
	0.4 wt.% Y	1028 ± 3.6	0.8 ± 0.04
700	0.1 wt.% Y	694 ± 3.4	9.8 ± 0.41
	0.2 wt.% Y	646 ± 1.2	10.6 ± 0.50
	0.4 wt.% Y	676 ± 0.7	9.3 ± 0.30
750	0.1 wt.% Y	532 ± 1.3	8.6 ± 0.32
	0.2 wt.% Y	556 ± 4.5	10.1 ± 0.43
	0.4 wt.% Y	528 ± 0.7	8.6 ± 0.38

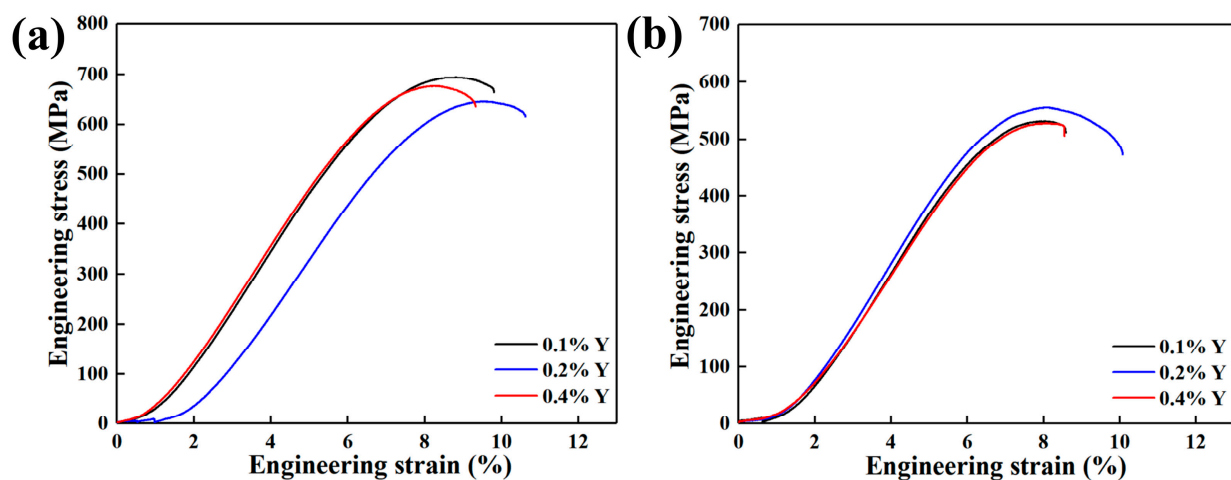
**Figure 17.** High-temperature tensile stress–strain curves of as-cast alloys with different Y content under different test temperatures: (a) 700 °C; (b) 750 °C.

Figure 18 shows the tensile fracture features of the as-cast alloys with different Y content at room temperature and high temperature. It can be seen that the fracture features of as-cast alloys at room temperature are mainly composed of larger cleavage planes and tearing edges, which are typical cleavage fracture modes, corresponding to brittle fracture. At high temperature, the fracture morphologies of as-cast alloys are the combination of number of dimples and partial tearing ridges, indicating that the plasticity of the alloy has been greatly improved.

The size and distribution of the precipitated phases will affect the mechanical properties of the alloys [31,32]. As described above, the size of Y_2O_3 in 0.1 wt.% Y composition alloy is small and dispersed, which has a certain dispersion strengthening effect in the alloy. With the increase of Y content, the size of Y_2O_3 increases, and a large-size brittle particle phase is formed in the local position. When the distribution of large-sized precipitates is uneven, it leads to more severe stress concentration and reduces strength during the tensile deformation of the alloy. This is also the reason for the large-size cleavage planes and tearing ridges in the 0.2 wt.% Y composition alloy. When the Y content increases to 0.4 wt.%, Y_2O_3 will be distributed more uniformly. At this time, Y_2O_3 forms a network structure distributed along the prior β grain boundary, which can improve the ability of the prior β grain boundary to hinder deformation and significantly reduce the weakening degree of the grain boundaries at high temperatures.

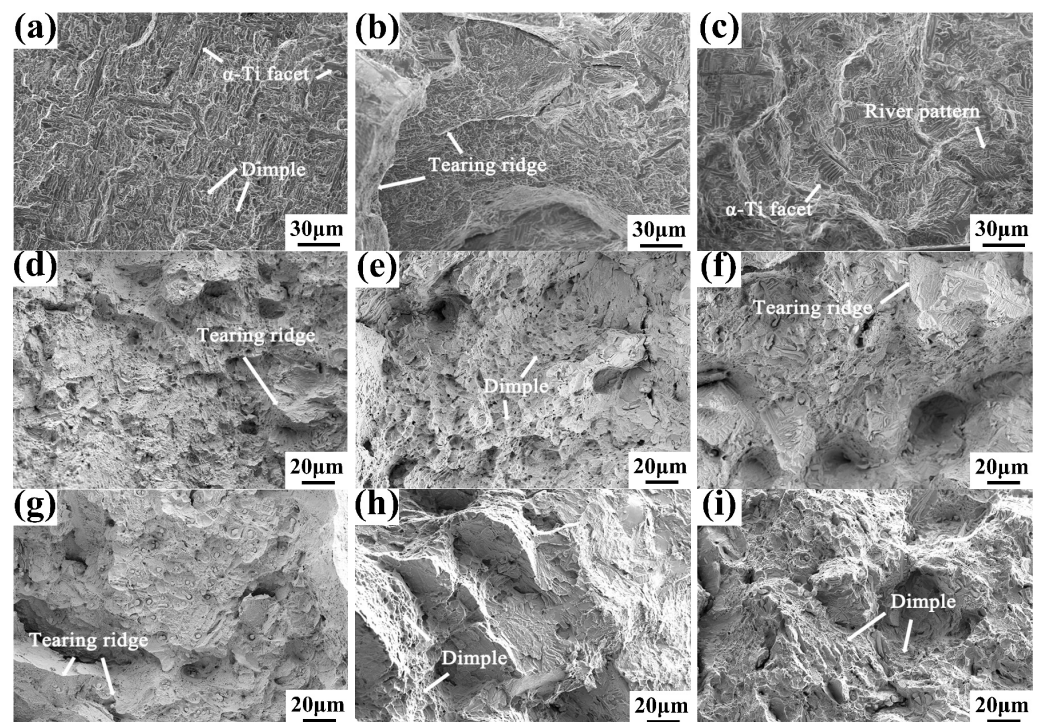


Figure 18. SEM images of tensile fracture of (a,d,g) 0.1 wt.% Y; (b,e,h) 0.2 wt.% Y; and (c,f,i) 0.4 wt.% Y alloys at (a–c) room temperature, (d–f) 700 °C and (g–i) 750 °C high temperatures.

In addition, the silicide in the microstructure will change the stress at the interface of α/β laths [33,34], and it synergistically affects the fracture strength and toughness of the alloy with the Y_2O_3 phase. Therefore, the mechanical properties of the alloys are affected by the distribution of the Y_2O_3 phase, silicide and temperature factors. A schematic illustration of the fracture mechanism of the alloys with different Y content is shown in Figure 19.

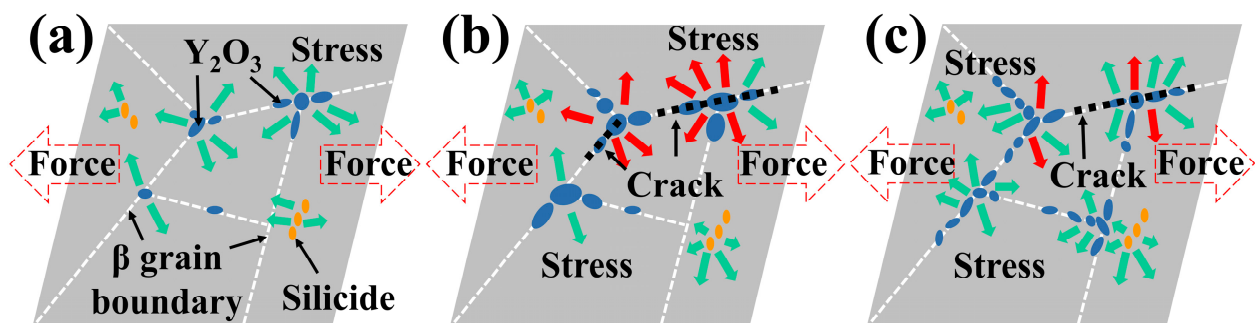


Figure 19. Schematic illustration of the fracture mechanism of the alloys with different Y content: (a) 0.1 wt.% Y; (b) 0.2 wt.% Y; (c) 0.4 wt.% Y.

4. Conclusions

- (1) The as-cast alloys with different Y content are mainly composed of α -Ti phase and a small amount of β -Ti phase. With the increase of Y content, both the α -Ti lattice parameters “a” and “c” increase.
- (2) The microstructures of the alloys are all of the widmanstätten structure, with typical basket weave features. The prior β grain size and α lamellar spacing decrease with the increase of the Y content.
- (3) With the increase of the Y content, the number of Y_2O_3 phases increases, and the morphologies of the Y_2O_3 phases change from short rod to long strip. The orientation relationships between the Y_2O_3 phase and α -Ti phase in 0.1 wt.% Y composition alloy are established as: $(002)_{Y_2O_3} // (\bar{1}120)_{\alpha-Ti}$, $[110]_{Y_2O_3} // [4401]_{\alpha-Ti}$.

- (4) $(\text{TiZr})_6\text{Si}_3$ silicide is precipitated from the β -Ti phase. It has an orientation relationship with the β -Ti phase: $(02\bar{2}1)_{(\text{TiZr})_6\text{Si}_3} // (011)_{\beta\text{-Ti}}$, $[\bar{1}2\bar{1}6]_{(\text{TiZr})_6\text{Si}_3} // [04\bar{4}]_{\beta\text{-Ti}}$.
- (5) The oxidation resistance of the alloys decreases with the increase of oxidation temperature and time. The 0.1 wt.% Y composition alloy has the best high-temperature oxidation resistance at different temperatures. The oxidation behaviors of the alloys conform to the linear-parabolic law, and the oxidation products of the alloy are composed of rutile-TiO₂, anatase-TiO₂, Y₂O₃ and Al₂O₃.
- (6) The room temperature UTS of the alloys decreases first and then increases with the increase of Y content; the 0.1 wt.% Y composition alloy has best room temperature mechanical properties, with a UTS of 1012 MPa and elongation of 1.0%. The UTS of the alloys at 700 °C decreases first and then increases with the increase of Y content, whereas the elongation shows an opposite trend. The UTS and elongation of the alloy with 0.1 wt.% Y is 694 MPa and 9.8%, showing an optimal comprehensive performance. The UTS and elongation of the alloys at 750 °C increase first and then decrease with the increase of Y content. The optimal UTS and elongation of the alloy is 556 MPa and 10.1%, obtained in 0.2 wt.% Y composition alloy. The cleavage and dimple fractures are the primary fracture mode for the room- and high-temperature tensile fracture, respectively.

Author Contributions: Conceptualization, B.F.; methodology, B.F.; validation, J.S., Y.W. and G.L.; formal analysis, J.L. (Jinkun Li); investigation, J.S.; resources, Y.W.; data curation, J.S. and T.D.; writing—original draft preparation, J.S. and G.L.; writing—review and editing, B.F. and J.L. (Jinhai Liu); visualization, T.D.; supervision, Y.W. and J.L. (Jinhai Liu); project administration, J.L. (Jinkun Li); funding acquisition, B.F. All authors have read and agreed to the published version of the manuscript.

Funding: This research was funded by the S&T Program of Tianjin under Grant No. 22YDTPJC00150.

Institutional Review Board Statement: Not applicable.

Informed Consent Statement: Not applicable.

Data Availability Statement: The data presented in this study are available on request from the corresponding author.

Conflicts of Interest: The authors declare no conflict of interest.

References

1. Hayat, M.D.; Singh, H.; He, Z.; Cao, P. Titanium metal matrix composites: An overview. *Compos. Part A* **2019**, *121*, 418–438. [[CrossRef](#)]
2. Zhao, E.T.; Sun, S.C.; Zhang, Y. Recent advances in silicon containing high temperature titanium alloys. *J. Mater. Res. Technol.* **2021**, *14*, 3029–3042. [[CrossRef](#)]
3. Li, C.Z.; Fu, B.G.; Dong, T.S.; Liu, J.H.; Song, Y.J.; Zhao, X.B.; Li, G.L. Microstructure and dry sliding wear behavior of as-cast TiC_p/Ti-1100-0.5Nb titanium matrix composite at elevated temperatures. *China Foundry* **2020**, *17*, 455–463. [[CrossRef](#)]
4. Lin, X.J.; Huang, H.J.; Yuan, X.G.; Wang, Y.X.; Zheng, B.W.; Zuo, X.J.; Zhou, G. High-temperature oxidation behavior of a cast Ti-47.5Al-2.5V-1.0Cr-0.2Zr alloy. *China Foundry* **2022**, *19*, 443–454. [[CrossRef](#)]
5. Li, J.; Xu, Y.Q.; Xiao, W.L.; Ma, C.L.; Huang, X. Development of Ti-Al-Ta-Nb-(Re) near- α high temperature titanium alloy: Microstructure, thermal stability and mechanical properties. *J. Mater. Sci. Technol.* **2022**, *109*, 1–11. [[CrossRef](#)]
6. Dai, J.J.; Zhu, J.Y.; Chen, C.Z.; Weng, F. High temperature oxidation behavior and research status of modifications on improving high temperature oxidation resistance of titanium alloys and titanium aluminides: A review. *J. Alloys Compd.* **2016**, *685*, 784–798. [[CrossRef](#)]
7. Lu, J.W.; Ge, P.; Zhao, Y.Q. Recent development of effect mechanism of alloying elements in titanium alloy design. *Rare. Metal. Mat. Eng.* **2014**, *43*, 775–779. [[CrossRef](#)]
8. Qu, S.J.; Tang, S.Q.; Feng, A.H.; Feng, C.; Shen, J.; Chen, D.L. Microstructural evolution and high-temperature oxidation mechanisms of a titanium aluminide based alloy. *Acta Mater.* **2018**, *148*, 300–310. [[CrossRef](#)]
9. Narayana, P.L.; Kim, S.W.; Hong, J.K.; Reddy, N.S.; Yeom, J.T. Tensile properties of a newly developed high-temperature titanium alloy at room temperature and 650 °C. *Mater. Sci. Eng. A* **2018**, *718*, 287–291. [[CrossRef](#)]
10. Yue, K.; Liu, J.R.; Zhang, H.J.; Yu, H.; Song, Y.Y.; Hu, Q.M.; Wang, Q.J.; Yang, R. Precipitates and alloying elements distribution in near α titanium alloy Ti65. *J. Mater. Sci. Technol.* **2020**, *36*, 91–96. [[CrossRef](#)]

11. Song, Y.J.; Fu, B.G.; Dong, T.S.; Li, G.L.; Wang, F.; Zhao, X.B.; Liu, J.H. Effect of Nb content on cyclic oxidation behavior of as-cast Ti-1100 alloys. *Materials* **2020**, *13*, 1082. [[CrossRef](#)]
12. Xu, Y.Q.; Fu, Y.; Li, J.; Xiao, W.L.; Zhao, X.Q.; Ma, C.L. Effects of tungsten addition on the microstructural stability and properties of Ti-6.5Al-2Sn-4Hf-2Nb-based high temperature titanium alloys. *J. Mater. Sci. Technol.* **2021**, *93*, 147–156. [[CrossRef](#)]
13. Tegner, B.E.; Zhu, L.; Siemers, C.; Saksl, K.; Ackland, G.J. High temperature oxidation resistance in titanium–niobium alloys. *J. Alloys Compd.* **2015**, *643*, 100–105. [[CrossRef](#)]
14. Shan, S.F.; Wang, H.; Zhang, B.; Jia, Y.Z.; Ma, M.Z. Influence of niobium and yttrium on plastic deformation energy and plasticity of Ti-based amorphous alloys. *China Foundry* **2021**, *18*, 60–67. [[CrossRef](#)]
15. Xiao, S.L.; Guo, Y.F.; Liang, Z.Q.; Wang, X.N.; Yang, J.K.; Wang, X.; Xu, L.J.; Tian, J.; Chen, Y.Y. The effect of nano-Y₂O₃ addition on tensile properties and creep behavior of as-cast TiAl alloy. *J. Alloys Compd.* **2020**, *825*, 153852. [[CrossRef](#)]
16. Liu, Z.G.; Zhang, C.J.; Chai, L.H.; Chen, Y.Y.; Woo, K.D. Effect of Y on microstructure and mechanical properties of α Ti alloy. *Mater. Sci. Forum* **2010**, *654–656*, 460–463. [[CrossRef](#)]
17. Zhong, X.Y.; Deng, T.S.; Xiao, W.L.; Zhong, M.; Lai, Y.H. Effect of minor Sc modification on the high-temperature oxidation behavior of near- α Ti alloy. *Corros. Sci.* **2023**, *217*, 111122. [[CrossRef](#)]
18. Sun, S.C.; Zhao, E.T.; Hu, C.; An, Y.K.; Chen, W.Z. Precipitation behavior of silicide and synergetic strengthening mechanisms in TiB-reinforced high-temperature titanium matrix composites during multi-directional forging. *J. Alloys Compd.* **2021**, *867*, 159051. [[CrossRef](#)]
19. Fu, B.G.; Wang, H.W.; Zou, C.M.; Wei, Z.J. The influence of Zr content on microstructure and precipitation of silicide in as-cast near α titanium alloys. *Mater. Charact.* **2015**, *99*, 17–24. [[CrossRef](#)]
20. Su, Y.; Hao, G.J.; Fan, H.Y.; Zhai, Y.W.; Kong, F.T.; Wang, X.P.; Chen, Y.Y. Study on rolling of a new near- α titanium alloy: Microstructure refinement and dual-scale silicides evolution. *J. Alloys Compd.* **2021**, *852*, 156867. [[CrossRef](#)]
21. Mathabathe, M.N.; Bolokang, A.S.; Govender, G.; Mostert, R.J.; Siyasiya, C.W. Structure-property orientation relationship of a $\gamma/\alpha_2/\text{Ti}_5\text{Si}_3$ in as-cast Ti-45Al-2Nb-0.7Cr-0.3Si intermetallic alloy. *J. Alloys Compd.* **2018**, *765*, 690–699. [[CrossRef](#)]
22. Wang, L.Q.; Xiao, B.; Zhao, S.Y.; Tan, P.; Li, Z.F.; Yin, J.O.; Shen, L.; Wang, J.Z.; Tang, H.P. Effect of Y addition on the microstructure and mechanical properties of the as-cast Ti-6Al-4V alloy. *Rare. Metal. Mat. Eng.* **2020**, *49*, 4142–4145.
23. Lee, H.S.; Yoon, J.H.; Yi, Y.M. Oxidation behavior of titanium alloy under diffusion bonding. *Thermochim. Acta* **2007**, *455*, 105–108. [[CrossRef](#)]
24. Xi, A.Y.; Zhuo, L.C.; Shao, H.; Shan, D.; Sun, F.; Lu, J.W.; Ji, K.L.; Chen, B.Q.; Zhao, X.H.; Wang, K.X. Oxidation kinetics and microstructure evolution of air oxidation behavior of TC18 alloy. *Vacuum* **2022**, *204*, 111332. [[CrossRef](#)]
25. Vaché, N.; Cadoret, Y.; Dod, B.; Monceau, D. Modeling the oxidation kinetics of titanium alloys: Review, method and application to Ti-64 and Ti-6242s alloys. *Corros. Sci.* **2021**, *178*, 109041. [[CrossRef](#)]
26. Kitashima, T.; Kawamura, T. Prediction of oxidation behavior of near- α titanium alloys. *Scr. Mater.* **2016**, *124*, 56–58. [[CrossRef](#)]
27. Berthaud, M.; Popa, I.; Chassagnon, R.; Heintz, O.; Lavková, J.; Chevalier, S. Study of titanium alloy Ti6242S oxidation behaviour in air at 560 °C: Effect of oxygen dissolution on lattice parameters. *Corros. Sci.* **2020**, *164*, 108049. [[CrossRef](#)]
28. Husson, E.; Proust, C.; Gillet, P.; Itié, J.P. Phase transitions in yttrium oxide at high pressure studied by raman spectroscopy. *Mater. Res. Bull.* **1999**, *34*, 2085–2092. [[CrossRef](#)]
29. Yu, H.H.; Li, S.Y.; Peng, S.Y.; Yu, Z.L.; Chen, F.Y.; Liu, X.T.; Guo, J.L.; Zhu, B.L.; Huang, W.P.; Zhang, S.M. Construction of rutile/anatase TiO₂ homojunction and metal-support interaction in Au/TiO₂ for visible photocatalytic water splitting and degradation of methylene blue. *Int. J. Hydrogen Energy* **2023**, *48*, 975–990. [[CrossRef](#)]
30. Fan, S.; Zhu, Y.H. Application of Van't Hoff equation to phase equilibrium. *Univ. Chem.* **2018**, *33*, 70–73. [[CrossRef](#)]
31. Chen, H.; Deng, H.; Liu, W.H.; Zuo, H.Y.; Zhou, L.J.; Qiu, W.B.; Wei, Y.Q.; Xia, Z.X.; Peng, H.Q.; Tang, J. Improving mechanical property of Ti55531 alloy by yttrium dopant. *J. Alloys Compd.* **2022**, *928*, 167122. [[CrossRef](#)]
32. Geng, K.; Lu, W.J.; Qin, Y.X.; Zhang, D. In situ preparation of titanium matrix composites reinforced with TiB whiskers and Y₂O₃ particles. *Mater. Res. Bull.* **2004**, *39*, 873–879. [[CrossRef](#)]
33. Xu, Q.; Fang, H.Z.; Wu, C.; Wang, Q.; Cui, H.Z.; Chen, R.R. Microstructure evolution and its effect on mechanical properties of cast Ti48Al6NbxSi alloys. *China Foundry* **2020**, *17*, 416–422. [[CrossRef](#)]
34. Fu, B.G.; Wang, H.W.; Zou, C.M.; Wei, Z.J. The effects of Nb content on microstructure and fracture behavior of near α titanium alloys. *Mater. Des.* **2015**, *66*, 267–273. [[CrossRef](#)]

Disclaimer/Publisher's Note: The statements, opinions and data contained in all publications are solely those of the individual author(s) and contributor(s) and not of MDPI and/or the editor(s). MDPI and/or the editor(s) disclaim responsibility for any injury to people or property resulting from any ideas, methods, instructions or products referred to in the content.